THESIS FOR THE DEGREE OF LICENTIATE OF PHILOSOPHY

From Multiple Scale Modeling to Multiscale-Modeling

Fabian Årén

Department of Physics

CHALMERS UNIVERSITY OF TECHNOLOGY

Gothenburg, Sweden 2021

From Multiple Scale Modeling to Multiscale-Modeling
Fabian Årén

© Fabian Årén, 2021.

Department of Physics
Chalmers University of Technology
SE-412 96 Gothenburg
Sweden
Telephone + 46 (0)31-772 1000

Cover:
A deep learning rendering of first a schematic 1st solvation shell, then a mesoscopic structure consisting of many solvation shells, and finally a bulk electrolyte.

Chalmers Digitaltryck
Gothenburg, Sweden 2021

From Multiple Scale Modeling to Multi-scale Modeling
Fabian Årén
Department of Physics
Chalmers University of Technology

Abstract

To power a sustainable future, interest in battery research and technology is at an all time high. In order to enable a transition to green tech many applications, such as the automotive industry, is in need of higher power densities, energy densities, longer life-times, and safer batteries.

One crucial component of batteries is the electrolyte, which for lithium-ion batteries (LIBs) have not developed as much as one would expect since its introduction in the 1990s. Through the use of novel electrolyte concepts such as highly concentrated electrolytes (HCE) and localized highly concentrated electrolytes (LHCE) desired qualities such as an increased energy density could be achieved. The effects of local properties on macroscopic behaviour within these systems are much more striking than conventional LIB electrolytes, constraining the use of common simulation techniques used in battery research.

This thesis studies these novel electrolyte concepts using an array of different computational methods, such as DFT, AIMD, and classical MD. Based on these techniques, as well as on the CHAMPION method, the work done in this thesis attempts to develop a method for tying together understanding of materials physics at the different scales represented by AIMD and classical MD through force sampling. This force sampling is presented as an alternative to commonplace MD force fields such as AMBER, CHARMM and GROMACS.
Finding the local structure important for explaining global transport phenomenon by showing that local HCE structure is retained when going from HCE to LHCE as well as showing the possibility for these new types of FFs, even though more work is needed on the accuracy of these FFs.

Keywords: lithium-ion batteries, machine learning, multi-scale modeling, electrolytes, DFT, AIMD, MD

Table of Contents

List of Tables and Figures **ix**

List of Publications **xi**

List of Abbreviations **xiii**

1 Introduction **1**

2 Batteries **3**
2.1 Electrochemical cells . . . 3
2.1.1 Li-ion Batteries . . . 3
2.1.2 Solid-Electrolyte Interphase . . . 5
2.1.3 Calcium Batteries . . . 6
2.2 Battery Properties . . . 6

3 Electrolytes **9**
3.1 Highly Concentrated Electrolytes . . . 9
3.2 Localised Highly Concentrated Electrolytes . . . 10
3.3 Ca^{2+} conducting electrolytes . . . 11
3.4 Ion Transport in Liquid Electrolytes . . . 11

4 Methods & Modelling of Battery Electrolytes **13**
4.1 DFT . . . 13
4.2 AIMD . . . 15
4.3 Classical MD . . . 17
4.4 Machine Learning Methods for Electrolyte Simulations . . . 18
4.4.1 Gaussian Process Regression . . . 19
4.5 CHAMPION . . . 19
4.6 Automated Force Field Finder . . . 20

5 Results & Discussion **23**
5.1 Ca^{2+} 1st Solvation Shells . . . 23
5.2 Local to Global Structure . . . 25
5.3 Generated Force Fields . . . 26

6 Conclusion & Outlook **31**

References **35**

List of Tables and Figures

2.1 Schematic of a typical Li-ion battery cell with a Cu current collector, a graphite anode, a 1 M $LiPF_6$ in EC/DMC electrolyte, a LCO cathode, and a Al current collector. 4
2.2 Schematic of an ESW. 5
2.3 Schematic of an SEI (▲, ■, ●) forming on the anode, protecting it from direct contact with the electrolyte whilst still allowing ionic transport. 6

3.1 Different charge transfer mechanisms at intermediate and high salt concentrations. 10

4.1 Multiple scale modeling vs multi-scale modeling. 13
4.2 Schematic of bonded and non-bonded parameters making up a classical FF. 18
4.3 Schematic Åvall plot linking the probability distribution of generalised forces to a generalised coordinate describing a interaction. Orange: Occupied bins. Blue: Empty bins 20

5.1 Use of DFT to elucidate the local structure in bulk electrolytes. . . . 24
5.2 The most common topologies around a Li cation in order of probability. Element colors: purple: Li, red: O, blue: N, grey: C, white: H, yellow: S, green: F. 25
5.3 Snapshots of the periodic simulation cell, highlighting the percolating network in a sea of solvent. 26
5.4 Comparing the quality of the generalised Åvall FF depend on number of bins. 27
5.5 The form of the Åvall FF after using the raw data as input to a Gaussian Process regression. The same physics is captured when studying the 1st half of a simulation as when studying the 2nd half. . . 28
5.6 The *statistical inefficiency* s dependence on Δt, the number of time steps $N_{timesteps}$, and the graph radius d. 29
5.7 The form of the Åvall FF after using the raw data as input to a Gaussian Process regression. Data with a statistical inefficiency $s = 21.1608$. 29

List of Publications

This thesis is based on the following Publications [1, 2, 3]. In the text they are referred to by their Roman numeral:

I. P.-A. Martin, F. Årén, and P. Johansson. Localized Highly Concentrated Electrolytes for Calcium Batteries. In manuscript

II. R Andersson, F Årén, A Franco, and P Johansson. Ion transport mechanisms via time-dependent local structure and dynamics in highly concentrated electrolytes. *Journal of the Electrochemical Society*, 167(14):140537, 2020

III. F. Årén, R. Andersson, and P. Johansson. Learning Force Fields from *Ab initio* Data. In manuscript

List of Abbreviations

ACN	Acetonitrile
AIMD	*ab initio* Molecular Dynamics
AM	Active Material
BOMD	Born-Oppenheimer Molecular Dynamics
CEI	Cathode Electrolyte Interphase
CN	Coordination Number
DFT	Density Functional Theory
DOD	Depth of Discharge
DSD	Dynamic Structure Discovery
ESW	Electrochemical Stability Window
FF	Force Field
GP	Gaussian Process
HCE	Highly Concentrated Electrolyte
HOMO	Highest Occupied Molecular Orbital
KPI	Key Performance Indicator
LCO	$LiCoO_2$
LE	Liquid Electrolyte
LHCE	Localized Highly Concentrated Electrolyte
LIB	Lithium-Ion Battery
LiTFSI	Lithium bis(trifluoromethanesulfonyl)imide
LP30	1 M $LiPF_6$ in EC/DMC
LUMO	Lowest Unoccupied Molecular Orbital
MD	Molecular Dynamics
ML	Machine Learning
NN	Neural Network
SCF	Self-Consistent Field
SEI	Solid-Electrolyte Interphase
SF	Symmetry Function
SHE	Standard Hydrogen Electrode
SN	Solvation Number
SOAP	Smooth Overlap of Atomic Position
SOC	State of Charge

1
Introduction

Materials are all around us. From the components in the electrical device you might be reading this text on to the paper of the printed version. Our modern world is built on the back of materials, and is propelled by humanity's increased understanding of the mechanisms and structures that give rise to all the unique and useful properties of different materials enabling the level of civilisation we have today.

Within the foreseeable future one of the most important research fields within materials science is the development of energy storage materials, such as the materials used to make batteries, which is a keystone in solving the climate issues [4] the human species will be facing within the coming century. Currently the state-of-the-art battery technology, the lithium-ion battery (LIB) has come a long way since its introduction in the 1990's by Sony [5]. Having an energy density of 200 Wh/l or 80 Wh/kg enabled the widespread adoption of handheld electronics. Today the energy densities have more than tripled.

One of the major problems of battery material research is the trial and error process used to discover new materials. Looking at trends in other fields [6, 7], it is clear that computational approaches have a great potential to be a solution. However, material simulations at the molecular level are difficult if directly trying to solve the Schrödinger equation, as it is a complex many body problem. One of the most effective techniques to simulate systems at this scale is density functional theory (DFT) [8]. Being able to simulate molecules accurately to achieve understanding quickly breaks down as the system size increases due to DFT lacking the ability to simulate dynamics, which becomes more important for explaining properties emerging at larger system sizes. Hence a conundrum appears; how to describe and simulate systems of any composition at a macroscopic scale with quantum accuracy. Paper **I** used DFT to identify the origins of spectroscopic observations and showcase the value of this method on a local scale.

Studying systems larger than a few molecules however requires a different tool set. Molecular dynamics (MD) simulations have been a functional tool since the 1950's [9, 10] and the method was the grounds for the 2013 Nobel Prize in Chemistry [11]. However, even though MD simulations have been shown numerous times to aid materials sceintists in their work [12, 13, 14], the method has several drawbacks, such as the method used to evaluate forces at each time step being non-trivial, as well as computationally expensive long range interactions. The umbrella term MD should be separated into two distinct methods, *ab initio* MD (AIMD), and classical

MD (from now on simply referred to as MD), both with their own distinct problems and benefits. Paper **II** display a proof-of-concept for a new method of analysing MD trajectories. Specifically AIMD is used to propagate a system, generating realistic structures, showcasing what AIMD in particular, and MD in general can be used for when studying batteries.

In order to enable MD simulations of non-conventional electrolytes on a nano-scale, a system for generating accurate force fields (FF's) have to be developed. Many attempts to circumvent this need have been made within the field of materials science in general, quite successfully, using a number of machine learning (ML) approaches, mainly using neural network (NN) approaches [15, 16, 17]. Even though ML techniques have gigantic upsides when it comes to computing hard-to-model problems there are certain drawbacks, such as the large data-sets needed for training, and the long times needed for learning, as well as the lack of understanding of why a model makes the predictions it does, colloquially called a "black box" [18]. Preferably a method to easily generate accurate FFs on the go for specific systems, without the drawbacks of conventional ML techniques, is needed. In paper **III** such a method is suggested through generalising the methods developed by Åvall and Johansson to exctract effective pair-wise forces and interaction energies from AIMD [19].

This thesis first shows how DFT and AIMD can be used to model electrolytes, at multiple scales, but foremost it proposes a novel method to generate FFs. All in order to study the rapidly changing landscape of modern battery electrolytes, in order to obtain properties such as transport numbers, current density, *etc.*, or to understand the structure of these materials, which can enable complementary and comparative information to experimental insights. The background for this thesis comes from studies of electrolytes using conventional computational methods, and discovering a gap in our ability to simulate complex systems at nano-scale, motivating the move from multiple scales to multi-scale modeling.

2
Batteries

2.1 Electrochemical cells

Electrochemical cells store chemical energy, which can be released as electrical energy through redox reactions. There are some miscommunication regarding the nomenclature of what a battery is, where battery can be used both to reference the electrochemical cell, as well as a battery pack. However in this thesis the word "battery" will refer to a battery pack, an assembly of cells and controlling electronics, as well as housing, fully capable of storing energy for large scale applications and in electric vehicles. Battery cells on the other hand are small single unit electrochemical cells, containing the reaction.

The cell is made up of four main components; 1) the anode, where oxidation occurs during discharge and electrons flow from, 2) the cathode, where reduction occurs during discharge, and electrons flow towards 3) the electrolyte, which is the charge carrying medium between the two electrodes, and 4) a separator which physically separates the electrodes to prevent a short circuit (Fig. 2.1). In addition to these components there are also current collectors, which are materials with high electronic conductivity, *e.g* metal foil, connecting the cell to an external circuit, as well as some sort of housing.

2.1.1 Li-ion Batteries

The most advanced battery chemistry in common use today are based on Li-ion technology. Li-ion batteries are popular due to both having high specific power and energy ($\sim$ 300 $\mathrm{Wkg^{-1}}$ and $\sim$ 150 $\mathrm{Whkg^{-1}}$ respectively at cell level for electric vehilce applications [20]) as well as a high voltage of $\sim$ 3 V against a standard hydrogen electrode (SHE) which is three times that of a typical Ni-Cd battery [21].

One of the most common traditional Li-ion battery chemistries is graphite and $LiCoO_2$ (LCO) used together with the $LiPF_6$ in EC/DMC (LP30) electrolyte. To understand contemporary battery technology this system is a good starting point. The ideal discharge reaction would be:

$$\begin{aligned}
&\text{Oxidation at anode:} && \mathrm{LiC_6 \rightarrow C_6 + Li^+ + e^-} \\
&\text{Reduction at cathode:} && \mathrm{Li^+ + e^- + CoO_2 \rightarrow LiCoO_2} \\
&\text{Total reaction:} && \mathrm{LiC_6 + CoO_2 \rightarrow C_6 + LiCoO_2}
\end{aligned}$$

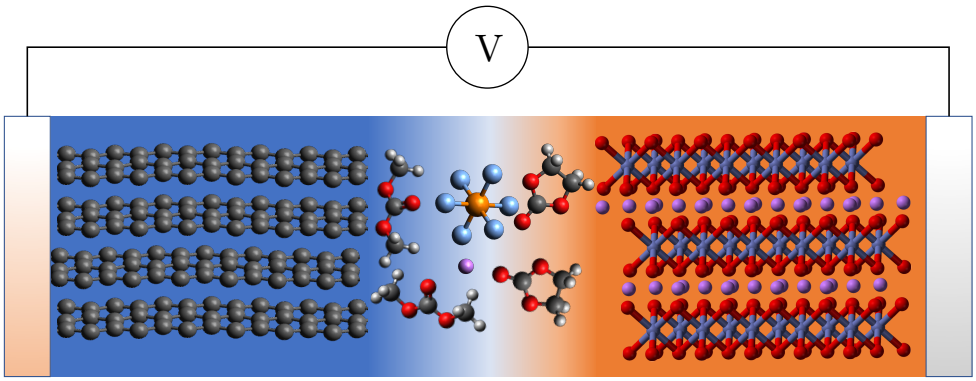

Figure 2.1: Schematic of a typical Li-ion battery cell with a Cu current collector, a graphite anode, a 1 M $LiPF_6$ in EC/DMC electrolyte, a LCO cathode, and a Al current collector.

By physically separating the oxidation and reduction reaction and connecting them through an external circuit cycling can be performed by transferring the electrons outside the cell, and the Li^+ through an electronically insulating medium, the electrolyte. From these reactions it is clear that the limiting factor of the amount of Li-ions that can be transported, and hence the energy content of the cell, is the Li^+, or an alternative charge carrier, storage capacity of both electrodes. This amount is given by the capacity Q, although since Q can be increased by simply increasing the electrode mass, which is not useful in most applications a more useful property to keep track of is the specific capacity C. Using Faraday's law the theoretical specific capacity, which puts an upper limit on the actual capacity can be calculated:

$$C_{th} = \frac{nF_0}{M_W}$$

where n is the number of electrons transferred during the reduction or oxidation reduction, F_0 is Faraday's constant, and M_W is the molecular weight of the active material (AM).

The theoretical voltage V_{th} is determined by the redox reactions taking place at the electrode. Given knowledge about the free energy of of the redox reaction, the theoretical voltage can be calculated as:

$$V_{th} = -\frac{\Delta G}{nF_0} = -\frac{\Delta G}{C_{th} M_W}$$

V_{th} gives an upper limit to the voltage. The actual cell voltage is given by, $V = E^+ - E^-$ where E^+ is the electrochemical potential at the positive electrode, and E^- is the electrochemical potential at the negative electrode, compared to a reference

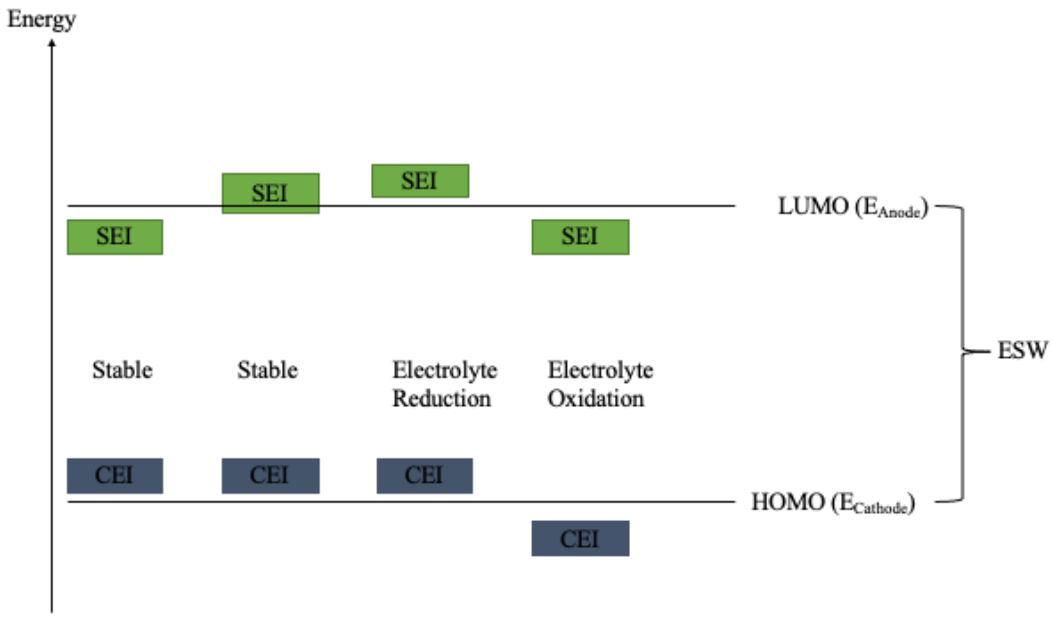

Figure 2.2: Schematic of an ESW.

electrode. Knowing the voltage at a charge Q, $V(Q)$ allows to calculate the electrochemical energy of the cell, given by:

$$E_{\text{chem}} = \int_0^C V(Q)\mathrm{d}Q$$

where C is the full capacity of the cell, the total amount of charge that can be reversibly transferred [22]. However when comparing batteries the more useful quantities are the volumetric and gravimetric energy density, which is calculated by dividing the total electrochemical energy by the volume, or the mass of the battery pack, the battery cell, or the AM, meaning batteries can be compared at three different levels.

2.1.2 Solid-Electrolyte Interphase

In order to keep a cell cycling the operating voltage needs to be less than the electrochemical stability window (ESW) (Fig. 2.2) of the electrolyte [23]. The ESW is defined as the potential difference between the highest occupied molecular orbital (HOMO) and the lowest unoccupied molecular orbital (LUMO). However battery systems such as LIBs operate with a voltage window outside the ESW. These systems continue operating through the decomposition of the electrolyte forming a passivating, yet still ionically conductive film on the anode (Fig. 2.3), called a solid-electrolyte interphase (SEI). The SEI is typically formed during the first couple of cycles on the anode by the reduction of the electrolyte. The oxidation products form the analogous cathode electrolyte interphase (CEI) on the cathode.

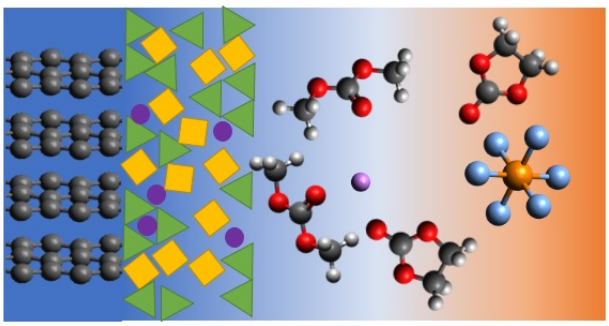

Figure 2.3: Schematic of an SEI (▲, ■, ●) forming on the anode, protecting it from direct contact with the electrolyte whilst still allowing ionic transport.

2.1.3 Calcium Batteries

State-of-the-art battery technologies, aka Li-ion based battery technologies, utilise a monovalent charge carrier. However this is not a fundamental limitation for a working battery concept. In recent years the interest for multivalent battery technologies, and especially calcium (Ca) batteries have risen [24, 25, 26]. The ability to drive multiple electron exchanges for every carrier transfer puts technologies such as these at comparable theoretical energy densities to Li-ion batteries [24], even though Ca^{2+} is a much larger ion than Li^{+}. This makes Ca-metal batteries a viable option for future more sustainable and cheaper batteries. The Ca metallic anode has a low redox potential of -2.87 V vs a SHE, meaning that all components in the electrolyte are at risk of reduction, forming different passivating layers. The problem hence is finding a solution allowing for both plating and stripping of Ca^{2+}.

Similarly cathode materials have to be developed also. A cathode needs to allow for high ionic mobility of the intercalating species. This can be achieved through using a host lattice where the diffusing ion is not coordinated to the lattice in its most thermodynamically stable configuration, as well as using a host structure with minor changes in ion coordination along the diffusion pathway [25]. Even though reversible Ca electrodeposition was demonstrated in 2016 [27] there are still a few hurdles to overcome before Ca batteries will become ready for market, *e.g.* the need to adapt the manufacturing process to be able to handle producing both Ca metal anodes and cells in an inert atmosphere, alternatively develop pre-passivated anodes.

2.2 Battery Properties

There are certain key performance indicators (KPI) important for comparing systems to keep track of when studying batteries. Important to all applications is knowing the energy content or *battery capacity* of the pack, as well as power, and the nominal cell voltage. Generally each unique battery system is designed to either optimise for

power or energy content depending on the intended use. Hence knowing a battery's power-to-energy-ratio can indicate what a battery system can be used for, however other aspects also play a role. The nominal cell voltage is the average voltage output of the cell, which drops as the system discharges, for current LIBs this can drop from 4.6V to 2.5V [28].

Hence to understand the live operation of a system the state-of-charge (SOC) defined as

$$\mathrm{SOC}[\%] = \frac{Q}{Q_{max}},$$

is needed, where the SOC represents the available charge in the system. Since the SOC tend to drop when cycling, this property is important for understanding the deterioration of the system. To understand the health of a battery cell the number of cycles also have to be known. To make sense of the cycling term it is easier to talk about equivalent full cycles. However this measurement lacks the ability to distinguish between one cycle of 100% of depth of discharge (DOD), two cycles of 50% of DOD, or ten cycles of 10% DOD. DOD is one of the largest contributors of battery degradation, determining the lifetime of the system. For example, Li-ion batteries undergo ten times more degradation when operated near 100% DOD compared to when operated at 10% DOD.

An almost equally important property for a cell is the Coulombic efficiency that quantifies the share of charges that are returned by the storage system, defined by:

$$\eta_{Coulombic} = \frac{\int_{period} I(t_{discharge})\mathrm{d}t}{\int_{period} I(t_{charge})\mathrm{d}t}$$

The Coulombic efficiency tends to decline when the battery is cycled, being one of the main reasons why batteries have a limited life span. One reason for such a degradation can be a parasitic reduction of electrode and electrolyte [29].

By studying materials at the cell level we can hope to develop systems that optimise these KPIs; *e.g.* increased energy and power content, as well as slower degradation. These indicators are tightly knit to the system dynamics, studied in paper **I** - **III**. The voltage of the system on the other hand is heavily dependent on the choice of chemistry, making the studies of different mono, and multivalent systems interesting.

3
Electrolytes

In a LIB the electrolyte, *e.g.* LP30, consists of solvents, and a solute, with the main purpose to transport charge carriers from one electrode to the other whilst remaining electronically insulating. Beyond ion transport the electrolyte has to adhere to many other criteria, such as the ability to wet the separator and electrodes, having a low flammability, low toxicity, and low environmental impact. In order to understand the charge transport in electrolytes it is important to study the mechanisms that facilitate transport, and what structures enable transport. The net transport of charges is driven by the difference in electrochemical potential between the electrodes. Even though this is the driving force on a macroscopic scale it is important to keep in mind the importance of both time and length scale. Herein we will discuss the importance of understanding the electrolyte structure at different scales in order to explain behaviour.

3.1 Highly Concentrated Electrolytes

Conventional electrolytes in modern batteries, such as the aforementioned LP30, are most often found at concentrations around 1 M. However since the early 2010's the interest for much higher salt concentrations in battery electrolytes have increased dramatically. The increased interest is due to some interesting properties displayed such as a lower solubility of transition metals dissolving from cathodes [30], higher rate capabilities [31, 32], and a widened ESW [31, 33]. The addition of more salt causes the electrolyte to have high ion density more akin to solvent in salt, than salt in solvent, making the electrolyte take on behaviour similar to ionic liquids. This also means that there is a low amount of free solvent in the liquid, which is one of the major identifiers of highly concentrated electrolytes (HCEs). Furthermore this leads to a higher density, higher viscosity, and a lower total ionic conductivity. Using a combination of experimental techniques Nilson et al. have shown that ionic conductivity depends more strongly on ionicity than viscosity [34], which is in agreement with the argument by Seo et al. [35]. In paper **II** we describe the mechanism behind the lower ionic conductivity for lithium bis(trifluoromethanesulfonyl)imide (LiTFSI) in acetonitrile (ACN) at a 1 : 2 molar ratio and show that a percolating network form from the anions and cations at such a high salt concentration whilst the solvent remains free. The lower ionic conductivity is explained by a decreased amount of transportation being conducted through a vehicular mechanism, which is defined as a cation in a shell of coordinated solvent molecules moving freely through the electrolyte (Fig. 3.1a), contrary to a

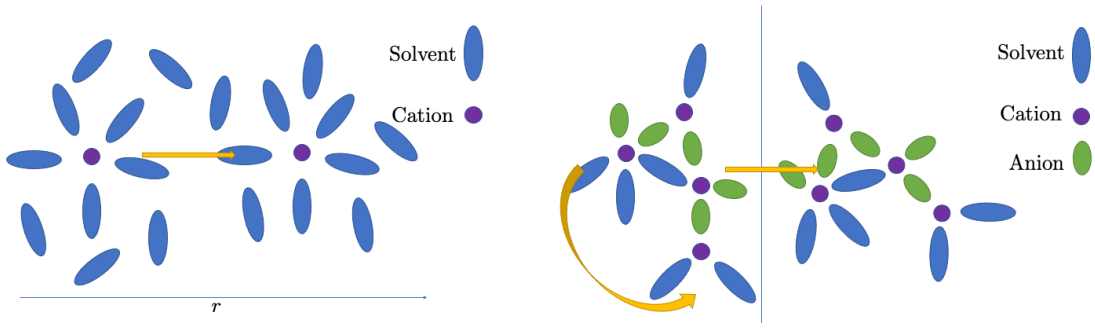

(a) How a solvent molecule shell forms a "vehicle" surrounding the cation and enabling transport through the solvent

(b) Rotating a structure containing cations can lead to a net charge transfer. This is an example of non-vehicular charge transfer.

Figure 3.1: Different charge transfer mechanisms at intermediate and high salt concentrations.

higher amount of non-vehicular transport, which is all type of transport that is not vehicular. This could for example be structural deformation, structural rotation, or jumping (Fig. 3.1b).

3.2 Localised Highly Concentrated Electrolytes

Localised highly concentrated electrolytes (LHCE) are designed to retain the positive qualities of HCEs, whilst improving the reduced ionic conductivity, that comes with an increased salt concentration. This is done by introducing a non-solvent, diluent, keeping the 1st solvent shell of the cation of the HCE intact. Hence it is globally similar to a liquid electrolyte (LE), but locally a HCE. The diluent oftentimes are some kind of ether, particularly fluoroethers as seen in the works of Qian et al [36], and Wang et al. [37, 38] . Given a shared local structure with HCEs the SEI forming abilities remain [39]. As recently seen the SEI formed from LHCE system are composed mainly of species coming from the anion decomposition and (near the surface) from the decomposition of diluent as well [40, 41]. Hence decomposition will occur using these systems, and the diluent has to be chosen accordingly, increasing the complexity of choice for electrolytes. All choices can be aided using computational means. For example: as preparatory work for paper **I** we screened many potential fluoroethers using DFT for their interaction energy against some standard acid in order to find out how inert their interaction is. Through this method a set of suitable candidates could be preselected and the scope of testing narrowed down. Similarly, MD is an additional method that could be used for screening [42]. The importance of computational methods for investigating LHCEs are even higher than for other electrolyte types due to properties of the diluent, since many diluents contain high amounts of flourine and the F - F interaction are important for many properties of these types of liquids. These interactions are hard to probe spectroscopically, leaving computational methods as a more effective choice.

3.3 Ca^{2+} conducting electrolytes

The work done in this thesis touches upon the problem of finding a good electrolyte for these types of systems. Currently $Ca(BF_4)_2$ salt and carbonate solvent electrolytes show a large ESW. However these system require operating temperatures above 100 °C in order to be reversible [27], severely limiting the commercial applications as well as the energy density of the system. At room-like operating temperatures THF based electrolytes can used to produce operating Ca cells. These types of electrolyte come with the drawbacks that the anodic stability is low ($\sim$ 3 V vs Ca^{2+}/Ca) which limits the selection of high voltage cathode materials [43], in turn lowering the cell energy density. Hence a viable middle ground has to be developed in order to make Ca-metal batteries a commercial reality. In paper **I** we investigate some possible special types of Ca electrolytes, and explore their structure using a combination of computational and experimental tools.

Ca-ion electrolytes are more affected by a low redox potential than Li-ion systems are. Since the Li-ion is $\sim$ 80 % the size of a Ca-ion and only carries half the charge it moves more freely though the passive layer formed on the electrode, and compared to other multivalent ions, Ca has a lower redox potential meaning other multivalent systems do not induce a SEI layer mitigating ion transport. Aurbach et al. showed that a wide range of Ca electrolytes form thick passivating films, making calcium plating impossible on both Ca and noble electrodes making Ca^{2+} mobility impossible [44]. Hence one of the main goals when studying calcium electrolytes is to develop a system allowing for both calcium plating and stripping at the anode.

3.4 Ion Transport in Liquid Electrolytes

A common cell works with a cell voltage of the order of magnitude of < 5 V, meaning that a Li^+ experiences an energy contribution of 5 eV. Operating at room temperature the thermal energy of the surroundings is $k_BT \approx 25$ meV. Hence, on a global scale bulk transport is driven completely by the voltage difference. Focusing on a local scale, assuming a thin separator (~ 20 μm) we see that linearly approximating cell voltage over separator thickness $\approx 2.5 \cdot 10^5$ Vm^{-1} over a typical distance of inter-molecular interaction ($\sim$ 5 Å), E = 0.125 meV. As a consequence the local dynamics is assumed to display motion uniformly distributed over all directions. In practice however the voltage profile is extremely steep near the electrode interfaces, making the importance of this potential more substantial there, and even less important than assumed here within the bulk, but that is outside the scope of this thesis.
The most important property for transport performance in a battery cell is the ion conductivity σ of the charge carrier, defined by:

$$\vec{J}^+ = \sigma^+ \vec{E}$$

relating the current density $\vec{J}$ of the charge carrier to the applied electric field $\vec{E}$. Generally σ is a tensor. In isotropic media such as liquid electrolytes however it is

reduced to a scalar.
Through the Nernst-Einstein equation, the ionic conductivity can be related to the diffusivity D^+, which for monovalent electrolytes (which will be used for demonstrative purposes here) takes the form:

$$\sigma^+ = \frac{cF}{RT} D^+,$$

where c is the salt concentration, F is Faraday's constant, R is the gas constant, and T is the temperature. Diffusivities tend to be easier to compute practically when simulating electrolytes, making this a more useful metric. The diffusivity can be approximated through the Stokes-Einstein equation:

$$D_i = \frac{k_B T}{6\pi\eta r_i},$$

where η is the dynamic viscosity of the electrolyte and r_i is the hydrodynamic radius of species i, typically on the order of $1 < r_i < 10$ Å in typical battery electrolytes [45]. In practice however the diffusion is calculated through a method such as mean squared displacement, or a Green-Kubo equation.

From the diffusivity two related, but distinct, and oftentimes confused concepts can be defined: the *transport number*, and the *transference number*. The *transport number* is defined as the fraction of the total current that is carried by the cation, *e.g.* Li^+, assuming no ion aggregation. Conversely the *transference number* is defined as the fraction of the migration current excluding currents due to concentration gradients, that is carried by the cations regardless of the speciation. The migration current is defined as the current driven by an electric field. What can be obtained from MD simulations however is neither of these concepts, but rather t^+, which is oftentimes also called the *transport number* defined as

$$t^+ = \frac{D^+}{D^+ + D^-}.$$

Even though the confusion in definitions of transport properties cause problems when comparing studies with each other, concentration trends, *etc.* seem to be consistent enough across methods. In paper **II** we study an array of transport properties using the newly developed CHAMPION software [46].

4

Methods & Modelling of Battery Electrolytes

This thesis focuses on the use of computational methods at multiple scales, ranging from molecular level methods such as DFT, to methods such as classical MD simulations, with AIMD in between (Fig. 4.1a). These methods provide vital information about the system of study, at the scale of the method. However for electrolytes it is important to also study the interconnectivity between the physics ranging from molecules and up. This concept is called multi-scale modeling, a field of science dedicated to studying and solving problems which have important features at multiple temporal and spacial scales [47](Fig. 4.1b). In papers **II** and **III** an attempt is made to marry the different scales and here a deeper explanation of the methods used will be given.

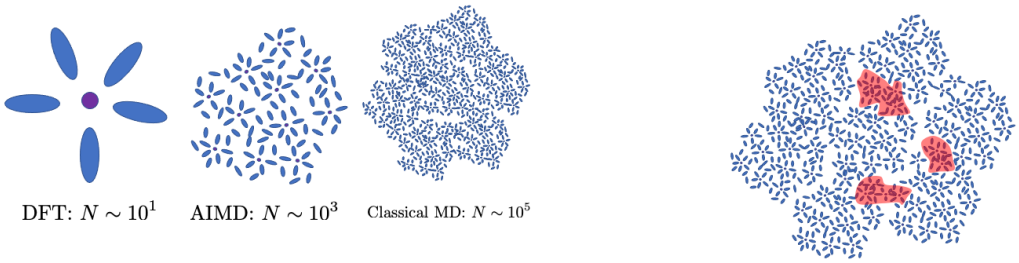

(a) Different computational techniques used at different scales.

(b) Local clusters in an electrolyte make up a global network.

Figure 4.1: Multiple scale modeling vs multi-scale modeling.

4.1 DFT

In paper **I** the local structures in CaB electrolytes were studied at the molecular level using DFT calculations, in order to supplement and explain experimental data. At the centre of DFT and other non relativistic quantum chemistry methods is solving the Schrödinger equation:

$$H\Psi(r,t,\sigma) = i\hbar\frac{\partial\Psi(\vec{r},t,\sigma)}{\partial t}$$

where Ψ is the wavefunction describing the system, H is the system's Hamiltonian, $\vec{r} = (x, y, z)$ all coordinates describing the system, and σ is the spin of the system. Neatly packaged like this it is easy to think that all physics is solved, but as *Paul Dirac* puts it [48]:

"The underlying physical laws necessary for the mathematical theory of a large part of physics and the whole of chemistry are thus completely known, and the difficulty is only that the exact application of these laws leads to equations much too complicated to be soluble."

This quote summarises the problem with modern materials science and chemistry, where the many-body-interactions necessary to describe the system quickly become too complex to be solved for systems larger than the hydrogen atom. Hence approximations of both the Hamiltonian and the wavefunction are needed to perform these calculations. Since a true representation of the wavefunction cannot be replicated on a classical computer [49], the first hurdle to overcome is to find an accurate representation of the wavefunction. Oftentimes single-electron wavefunctions, and molecular orbitals Φ_n are written using a basis set of functions φ_μ centred on the nuclei. The basis set functions are usually a linear combination of Gaussian functions

$$\varphi_\mu = \sum_\mu d_\mu g(\xi, r)$$

where d_μ is a scale factor and

$$g(\xi, r) = C x^{n_i} y^{m_i} z^{l_i} e^{-\xi_i r^2}$$

where C is a normalisation constant, n_i, m_i, l_i determines the type of orbital the function represent (s, p, d, etc.). Following the creation of a basis set ($\{\varphi_\mu\}$) molecular orbitals can be defined as:

$$\Phi_k = \sum_\mu c_{k,\mu} \varphi_\mu$$

Solving the Schrödinger equation is done through systematically making better guesses for the wavefunction $\Psi(r_1, r_2, \ldots, r_n; R_1, R_2, \ldots, R_N) = \sum_k a_k \Phi_k$. What is solved for are the values of all coefficients a_k, enabling the energy $\epsilon = \langle \Psi | H | \Psi \rangle$to be calculated. Since the variational principle states that $E_0 < \epsilon$, where E_0 is the system's ground state energy, it is possible to iterate systematically finding better and better solutions to the wavefunction using an array of methods.

In this thesis DFT has been used as the method to find the ground state of a number of systems. Through two theorems postulated by Hohenberg and Kohn, DFT is used to identify a system's ground state through the electron density rather than its wavefunction, reducing the number of coordinates needed to describe the system from $3(n + N) - 6$ to 3.

The two Hohenberg-Kohn theorems are:

1. *The ground state electron density uniquely determines the external potential of the system, and thus the whole Hamiltonian.*
2. *A universal functional, valid for any external potential, can be defined in terms of only the electron density.*

Using these two theorems the energy of the ground state of the system can be calculated from the elctron density:

$$E_0 = T[n(r)] + \int_{R^3} V_{nuclei}(r)n(r)\mathrm{d}r + \frac{1}{2}\frac{1}{4\pi\epsilon_0}\int_{R^3}\frac{n(r)n(r')}{|r-r'|}\mathrm{d}r\mathrm{d}r' + E_{xc}[n(r)]$$

where $T[n(r)]$ is the kinetic energy functional of a non-interacting electron gas, V_{nuclei} is the potential caused by the nuclei, and $E_{xc}[n(r)]$ is the exchange correlation functional containing the remaining energy in the interaction [50]. Using the Kohn-Sham equation:

$$\left(-\frac{\hbar^2}{2m_e}\nabla^2 + V_{eff}(r)\right)\Psi_i(r) = \epsilon_i\Psi_i(r)$$

where

$$V_{eff} = V_{nuclei}(r) + \frac{1}{2}\frac{1}{4\pi\epsilon_0}\int_{R^3}\frac{n(r')}{|r-r'|}\mathrm{d}r' + \frac{\delta E_{xc}[n(r)]}{\delta n(r)}$$

enables the electron density to be determined using a self-consistent field (SCF) approach. The term $\frac{\delta E_{xc}[n(r)]}{\delta n(r)}$, called the exchange-correlation potential $V_{xc}[n(r)]$ is approximated differently by the various DFT functionals. Generally V_{xc} is approximated by it being expanded in terms of electron density. There are functionals ranging from simple and computationally inexpensive to very accurately and expensive ones. In paper **I** the Minnesota functional M06-2X [51] has been used for the most part, with some simulations done using the B3LYP functional [52]. The Minnesota functionals are a group of parametrised exchange correlation energy functionals, based on the meta-GGA approximation meaning they include terms including the energy density, as well as it's first and second derivatives. B3LYP on the other hand is a less complex, GGA correlation function, simply containing information of the energy density and the first derivative. However even though DFT is considered accurate the computational cost scales cubically with the number of atoms in the system, making simulations of a single solvation shell the most common in the field of electrolytes. These typically target properties such as HOMO/LUMO levels, vibrational modes and frequencies, and their associated IR intensities as well as Raman activities *etc.*

4.2 AIMD

In paper **II** larger systems consisting of several solvation shells forming larger structures are studied using AIMD. In order to update the atomic positions the force acting on the atom has to be identified. The Hellmann-Feynman theorem shows that the force acting on a particle i is simply determined by the electron density as well as

the Coulomb interaction between the nuclei:

$$F = -\frac{\partial E}{\partial R_i} = -\left\langle \Psi \left| \frac{\partial H}{\partial R_i} \right| \Psi \right\rangle = Z_i \left(\int n(r) \frac{r - R_i}{|r - R_i|^3} \mathrm{d}r - \sum_{j \neq i}^{N} \frac{Z_j (R_j - R_i)}{|R_j - R_i|^3} \right).$$

Therefore using similar methods for identifying the electron density as in DFT all forces acting within the simulation system can be identified. Knowing all the forces, the system can be propagated through time by solving Newtons second law, and updating all particles position. One of the most common algorithms for updating positions in MD methods is the Velocity-Verlet algorithm [50]. Updating positions with a half-step the algorithm looks as follows:

1. $\vec{v}(t + \frac{1}{2}\Delta t) = \vec{v}(t) + \frac{1}{2}\vec{a}(t)\Delta t$
2. $\vec{x}(t + \Delta t) = \vec{x}(t) + \vec{v}(t + \frac{1}{2}\Delta t)\Delta t$
3. Derive $\vec{a}(t + \Delta t)$ for the updated positions $\vec{x}(t + \Delta t)$
4. $\vec{v}(t + \Delta t) = \vec{v}(t + \frac{1}{2}\Delta t) + \frac{1}{2}\vec{a}(t)\Delta t$

Where step 3 is non-trivial. Deriving new accelerations at each iteration means solving a conventional matrix diagonalisation for an updated electron density with each updated position, as is done when using Born-Oppenheimer molecular dynamics (BOMD). This is computationally expensive when done at every time step, making this approach risible for even moderate scale systems [50].

An alternative approach to combine the quantum mechanical way to derive the forces acting in the system with classical MD was done by Car and Parrinello in 1985 [53]. By treating the total energy in the system as a functional of the electronic wave function and nucleic positions:

$$E_{tot} = E_{tot}[\{\psi_i\}, \{\vec{R}_j\}]$$

in combination with the fact that the electronic wavefunctions are orthonormal $\langle \psi_i | \psi_j \rangle = \delta_{ij}$ Car and Parrinello were able to compute the total energy. They did this by using the variational principle, minimizing $E_{tot}[\{\psi_i\}, \{\vec{R}_j\}]$, instead of computing the electronic structure at every step of the MD simulation, as the nucleic positions are varied simultaneously as the electronic orbitals. In order to propagate the system in time and give the electrons a kinetic energy, a fictitious time dependence is given to the wavefunction, which allows the following classical Lagrangian to be constructed:

$$L(\{\psi_i\}, \{\vec{R}_j\}) = \frac{\mu}{2} \sum_{i=1}^{n} |\dot{\psi}_i|^2 + \frac{1}{2} \sum_{j=1}^{N} M_j \dot{\vec{R}}_j^2 + E_{tot}[\{\psi_i\}, \{\vec{R}_j\}] + \sum_{kl} \Lambda_{kl} \langle \psi_k | \psi_l \rangle$$

where μ is a fictitious electron mass. The fictitious mass should be small enough such that the Born-Oppenheimer approximation still holds and the electronic wavefunction adapts to the position of the nuclei, whilst at the same time being large enough to allow for relatively large time steps. A typical choice for $\mu = 400\ m_e$, which is what we have used. Beyond the introduction of a fictitious mass, Lagrangian multipliers Λ_{kl} are introduced as to fulfil any external constraints, *e.g* retaining orthonormality

of the Kohn-Sham orbitals at each time step. Solving for the classical equations of motion yield:

$$\mu\ddot{\psi}_i = -\frac{\delta E_{tot}}{\delta \psi_i} + 2\sum_j \Lambda_{ij}\psi_j \tag{4.1}$$

$$M_j\ddot{\vec{R}}_j = -\frac{\delta E_t ot}{\delta \vec{R}_j} + \sum_{kl} \Lambda_{kl}\frac{\delta \langle \psi_k | \psi_l \rangle}{\delta \vec{R}_j} \tag{4.2}$$

which are implemented in CPMD [54], the software used to generate data for analysis in paper **II**, and to generate training data in paper **III**.

4.3 Classical MD

Unlike AIMD where the forces are derived from the electron density and Coulombic interactions between nuclei, classical MD calculate the interatomic forces using a FF, which is a set of parameters and functions, together forming a potential energy surface where the total system energy is determined by the atomic positions $\left\{\vec{R}_j\right\}$. The energy is most often given by, but not limited to the form:

$$E_{tot} = 4\sum_{ij}\epsilon_{ij}\left[\left(\frac{\sigma_{ij}}{r_{ij}}\right)^{12} - \left(\frac{\sigma_{ij}}{r_{ij}}\right)^{6}\right] + \frac{1}{4\pi\epsilon_0}\sum_{ij}\frac{q_i q_j}{r_{ij}}$$
$$+ \sum_{\text{bonds}}\frac{k_b(l-l_{0,b})^2}{2} + \sum_{\text{bond angles}}\frac{k_a(\theta-\theta_{0,a})^2}{2} + \sum_{\text{dihedrals}}\sum_{n} k_{n,d}\cos(n\phi+\phi_{0,n}).$$

where the first term is the Lennard-Jones approximation describing the Pauli exclusion principle and the van der Waals interactions, the second term is the Coulomb interaction between all pairs of atoms. Term three to five are all bonded interactions modelled as Hooke's law for two body objects, an angle potential defined by the angle between three bound bodies, and a proper/improper torsion potential defined by the angle between the planes formed between four bonded atoms. This form for the energy term (Fig. 4.2) is used in common FFs such as Amber [55], CHARMM [56], and GROMACS [57]. From this form the FF parameters are the set of $\{\epsilon_i, \sigma_i, q_i, k_{b,i}, l_{0,b,i}, k_{a,i}, \theta_{0,b,i}, k_{n,d,i}, \phi_{0,n,d,i}\}$ where $\sigma_{ij} = \frac{\sigma_{ii}+\sigma_{jj}}{2}$, $\epsilon_{ij} = \sqrt{\epsilon_{ii}\epsilon_{jj}}$, and σ_{ii} is the distance at which the particle-particle potential energy is zero, ϵ_{ii} is the depth of the potential well. Conventionally FF parameters are developed using a combination of quantum chemistry computations of single molecules in vacuum, and experimental data, often of thermodynamic nature. However, since FF parameters are often validated by their ability to predict thermodynamical properties through experimentally obtained values it is not guaranteed that a given FF accurately represents local dynamics, even if the parameter set accurately recreates experimental values.

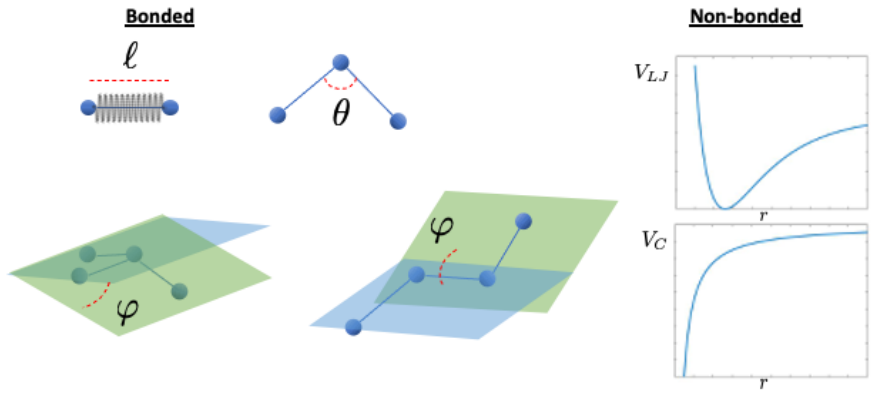

Figure 4.2: Schematic of bonded and non-bonded parameters making up a classical FF.

4.4 Machine Learning Methods for Electrolyte Simulations

There is a strong push to understand complex materials such as new electrolytes. One method used to tackle this problem has been machine learning (ML), with a recent surge in methods bridging the realm between AIMD and classical MD simulations. ML used to describe materials structure began in 2007 when Behler and Parinello [58] developed symmetry functions (SF), creating transferable neural network (NN) potentials through the chemical locality around an element. Similarly in 2013, Bartók *et. al.* developed the Smooth Overlap of Atomic Position (SOAP) directly defining the similarity between any two atomic neighbourhood environments, enabling the development of interatomic potentials through the GAP framework [59, 60]. Other alternatives to develop interatomic potentials have been through different NN approaches, such as SchNet [61]. More concretely relevant for electrolyte applications, Wang *et. al.* for example have developed a NN based on SchNet, learning chemical embeddings for elements in ionic liquids and new electrolytes [62]. Alternatively NN such as PiNet [63] can be used to learn electronic multipoles of atomistic simulated liquids [64].

Common for almost all ML approaches, especially those based on NN is the need for extensive amounts of data for training and testing of models, making the need for available data more important than ever. This need can be seen in contemporary projects such as BIG-MAP [65] as well as the Materials Genome Initiative [66] trying to standardise data presentation as well as making it available to a wider audience.

4.4.1 Gaussian Process Regression

A method for interpolation of data given a sparse set of data points is Gaussian Process regression (GP), commonly known as Kriging. GP regression is used to predict a function value at a given point by computing the weighted average of the known values of the function in the neighbourhood of the point. This means that a GP is completely specified by a mean function and a positive definite covariance function. Given a set of inputs $x^{(1)} \cdots x^{(n)}$, a mean function $\langle f(x) \rangle = 0$, and a covariance function $K_{p,q} = \mathrm{Cov}\left(f(\mathbf{x}^{(p)}), f(\mathbf{x}^{(q)})\right) = K\left(\mathbf{x}^{(p)}, \mathbf{x}^{(q)}\right)$, a joint distribution may be defined

$$f(\mathbf{x}^{(1)}) \cdots f(\mathbf{x}^{(n)}) \sim \mathcal{N}(\mathbf{0}, K).$$

Given this knowledge a GP can be obtained using Bayesian linear regression:

$$f(\mathbf{x}) = \mathbf{x}^T \mathbf{w}$$

where the weights $\mathbf{w} \sim \mathcal{N}(\mathbf{0}, \Sigma_p)$. Hence the mean function is given by:

$$\mathbf{E}\left[f(\mathbf{x})\right] = \mathbf{x}^T \mathbf{E}[\mathbf{w}] = 0$$

and the covariance function is given by:

$$\mathbf{E}\left[f(\mathbf{x}) f(\mathbf{x}')\right] = \mathbf{x}^T \mathbf{E}[\mathbf{w}\mathbf{w}^T]\mathbf{x}' = \mathbf{x}^T \Sigma_p \mathbf{x}'.$$

The Bayesian linear regression is based on Bayes theorem:

$$P(\mathbf{y}|X, \theta) \propto P(\theta) P(\theta|X, \mathbf{y})$$

Where $P(\theta)$ is known as the prior, representing the assumption of the probability of a set of parameters θ prior to knowledge of data, and $P(\theta|X, \mathbf{y})$ is known as the likelihood, representing the probability of observing the parameters θ given knowledge about the data $X, \mathbf{y}$, and $P(\mathbf{y}|X, \theta)$ is the posterior of the given hypothesis explaining the data. Commonly θ is chosen by optimising the marginal log-likelihood:

$$\log P(\mathbf{y}|X, \theta) = -\frac{1}{2} \log |K(X, X) + \sigma^2| - \frac{1}{2} \mathbf{y}^T (K(X, X) + \sigma^2)^{-1} \mathbf{y}$$

through sampling the probability space of possible θ.

4.5 CHAMPION

In paper **II** as well as Andersson *et. al.* [46] an algorithm for structure detection has been created. Through dynamic structure discovery (DSD), finding and analysing what moves together within a simulation, the CHAMPION software is capable of detecting a global bond graph for the system that uniquely determines its bond topology. This bond graph is later able to be subdivided into components such as ionic aggregates and molecules, or into solvation shells. Through knowing all bonds within a simulation, as well as all solvation shells and other structure, we are capable of of sorting all data provided in the simulation in new unique ways providing us with understanding of emergent structures within materials as well as giving insights into the dynamics of the system.

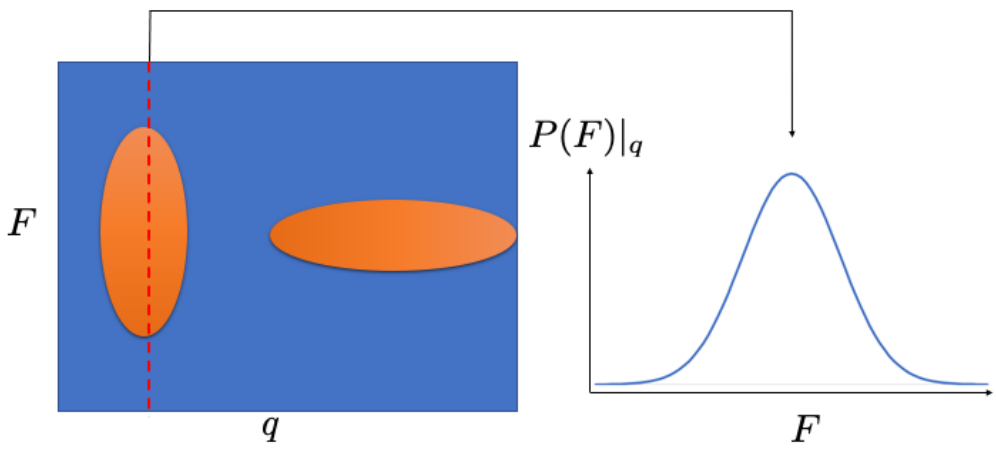

Figure 4.3: Schematic Åvall plot linking the probability distribution of generalised forces to a generalised coordinate describing a interaction. Orange: Occupied bins. Blue: Empty bins

4.6 Automated Force Field Finder

In paper **III** we propose a new light-weight method for generating system specific FFs. Being inspired from the work of Åvall and Johansson (2020) [19] where they investigated the force distribution between a solvation shell and a central atom in terms of centre-of-mass coordinates, we herein develop a similar method by generalising the Åvall method of binning central forces depending on distance to binning the interaction strength related to each interaction type. The interaction types used are the same as in conventional FFs, with 2-, 3-, and 4-body bonded interactions, as well as an electrostatic term and a Lennard-Jones like term. In this method however the long range electrostatic and dispersion interactions are treated together and will henceforth be referred to as the pairwise interaction. By first running small first principle MD simulations, the forces acting between all particles of a system type can be found. Then projecting the generalised force acting on all particles partaking in an interaction type based on a CHAMPION bond graph, against a generalised coordinate q describing said interaction, a 2D histogram of distributions (Fig. 4.3) are formed.

These 2D histograms contain all information about said effective interaction, *e.g.* between two carbon atoms, where effective interaction denotes the distributions of interactions in the presence of environmental noise assumed to be normally distributed with zero mean. Having this method based upon the CHAMPION bond-graph identifying method [46] also enables a FF that treats different bond types separately, *e.g.* separating linearly bonded carbon from cyclically bonded carbon. Such distinctions have been shown to be useful in other, more conventional, FFs such as AMBER and GROMACS [55, 57].

From the positions of and forces acting on each atom, both the generalised coordinates and forces can be computed and sampled. The statistical distributions of generalised forces as functions of the corresponding generalised coordinates result from a combination of the effective interaction between the atoms involved, and effects of the background. The approach taken here is based on assuming the background effect to be unbiased noise, so that the mean of the sampled distributions estimates the true effective interaction.

Knowing the positions and forces acting on each particle within a trajectory, generalised coordinates and generalised forces can be computed and sampled. The distributions of generalised forces as function of the corresponding generalised coordinates give rise to a 2D histogram similar to an Åvall plot. These histograms contain the information about the effective interaction between all particles involved, as well as the effective background.

Given a force distribution $\mathcal{F}|_q$ of generalised forces $\{F_i(q)\}$ as seen in Fig. 4.3, where $i \in \{0, \text{number of samples of interaction type}\}$ one can show that the specific force $F_i(q)$ can be written as:

$$F_i(q) = F(q) + \Delta f$$

where $F(q)$ is the true generalised interaction strength and Δf is a stochastic background noise. Assuming that the noise is Gaussian:

$$\begin{aligned}
\sum_i^N F(q) &= \sum_i^N F_i(q) - \sum_i^N \Delta f \\
&\Rightarrow \\
NF(q) &= N \langle F_i(q) \rangle - N \langle \Delta f \rangle \\
&\Leftrightarrow \\
F(q) &= \langle F_i(q) \rangle .
\end{aligned}$$

Hence any interaction described using the generalised Åvall method should be reproducible given the mean force value at any point along the generalised coordinate axis.

Given the sparse but spread out nature of the data produced this way, a smooth function filling the space between data points can be generated using GP regression. This pairs well with the reactive capability provided by having the method based upon the CHAMPION method. The FF identified can be made reactive through computing bond likelihood functions as a function of distance. Hence it is possible to determine on a snapshot-by-snapshot basis which atoms in the system are bonded in, one, two, three, or even four of the four bond types previously discussed. This possibility enables the look-up tables to be dynamically chosen during the simulation, enabling a great amount of customiseability to the interactions.

5

Results & Discussion

Here the results of the appended papers **I** - **III** are briefly presented and discussed. These move from the molecular level using DFT methods to determine the Raman spectra of solvation shells (paper **I**), to the microscopic scale where AIMD is used to equilibrate what structures form in a HCE (paper **II**), and these are finally tied together through the use of the newly developed CHAMPION [46] bond graph discovery algorithm and the generalised Åvall method (paper **III**).

5.1 Ca^{2+} 1st Solvation Shells

In order to explain experimental results depending on local structure computational methods are useful. In paper **I** we calculate the Raman spectra of a wide set of Ca^{2+} 1st solvation shell structures in order to elucidate the local structure within Ca^{2+} HCEs and LHCEs. Artificial Raman spectra are calculated from which it is clear that free PC, $[Ca(PC)_4]^{2+}$, free TFSI, and $[Ca(TFSI)_2]$ all play an important role (Fig. 5.1). These structures are limited in complexity by both the capabilities of the DFT method as well as the researchers' intuition, which puts limitations to the predictions possible to make for complex materials.

By investigating a wide suit of structures of the form $[Ca((TFSI)_N PC)_M]^{(N-2)-}$, where N is the number of TFSI ions surrounding a central Ca-ion, and M is the number of PC molecules surrounding said Ca ion, in paper **I** the main peaks in the region of interest could be identified as the ones mentioned (Fig. 5.1c). From the combination of experimental Raman data and computational DFT data we could confirm that the first solvation shell is retained when diluting a HCE, creating a LHCE, making this a viable approach when searching for Ca-electrolytes that have the potential for SEI formation, and cycle at room temperature. By understanding the local structure the design of electrolytes can be aided. DFT works well as a complimentary method to Raman spectroscopy, however to make predictions about structure DFT is not the most optimal method since the input structure is what gets tested, making it a cumbersome approach to make predictions based on the full structure space. Hence in order to understand fully unknown materials, methods such as MD can provide a better fit.

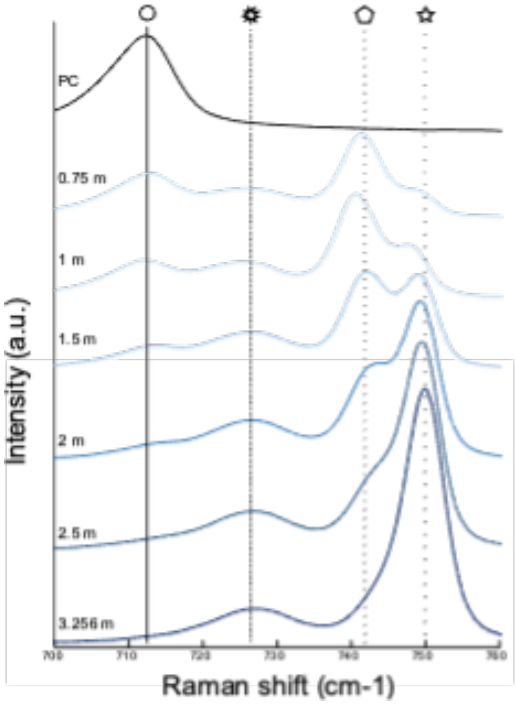

(a) Band assignments of HCE and LE through the use of DFT (symbol key subFig. 5.1c).

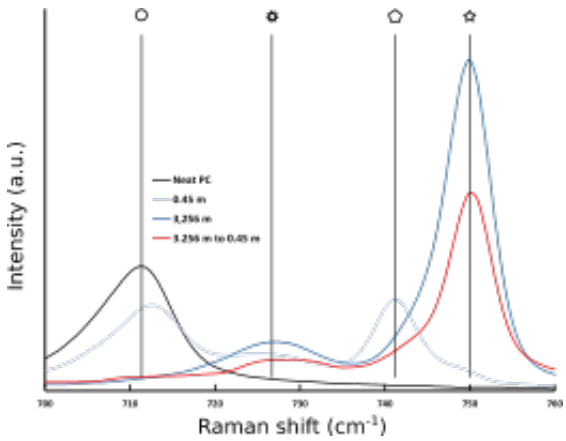

(b) Band assignment when diluting HCE from 3.256 m to a nominal 0.45 m LHCE (symbol key subFig. 5.1c).

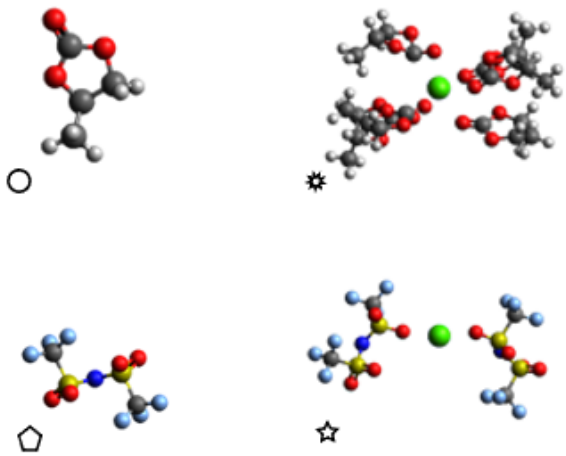

(c) A symbol key to 5.1a and 5.1b . Free PC (○), $[Ca(PC)_4]^{2+}$ (✹), free TFSI (⬠), $[Ca(TFSI)_2]$ (☆).

Figure 5.1: Use of DFT to elucidate the local structure in bulk electrolytes.

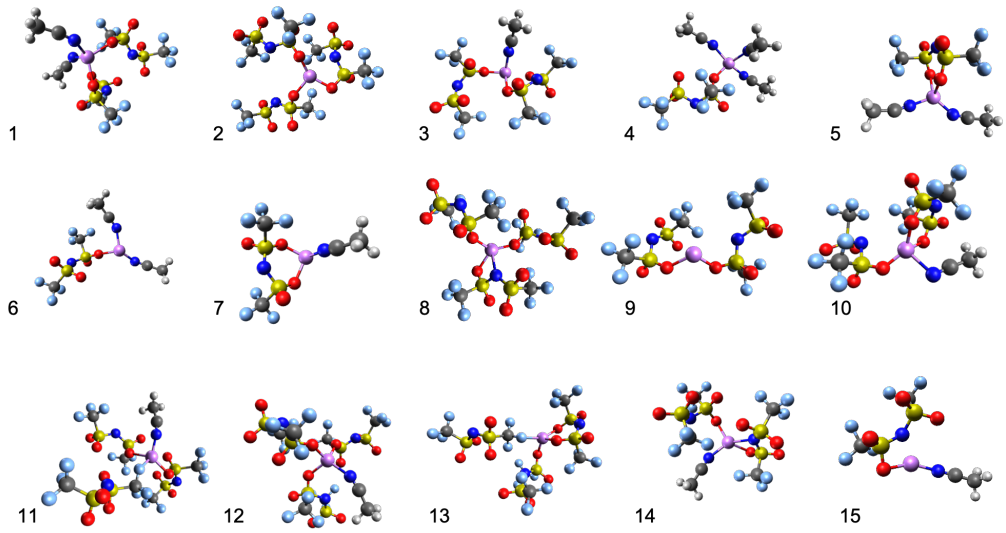

Figure 5.2: The most common topologies around a Li cation in order of probability. Element colors: purple: Li, red: O, blue: N, grey: C, white: H, yellow: S, green: F.

5.2 Local to Global Structure

In paper **II** we identify how to use the newly developed CHAMPION method together with AIMD simulations to gain knowledge of both the local and global electrolyte structure. AIMD enables simulations where the local interactions are replicated accurately, as can be observed with the coordination number (CN) for $Li^+ \approx 4$, which is common for LIB electrolytes based on small organic molecules, regardless of composition [67, 68]. In many electrolytes CN is similar to the solvation number (SN) since almost all coordinations are monodentate. This is, however, not true for LiTFSI in ACN at higher concentrations where the SN is closer to 3, even though the CN remains close to 4 due to more bidentate TFSI coordination by Li^+, which concurs with other studies [69]. These results are reflected in the common topologies (Fig. 5.2) found in the simulation.
On a global scale we see that these structures form a percolating network, in a sea of free solvent (Fig. 5.3), which is in sharp contrast to the common conception about HCEs, where its unique behaviour is believed to stem from a lack of free solvent [70].
The accuracy of this analysis scales with the number of ions and even for a concentrated system such as this, system size and trajectory length are both on the smaller scale in order to say something with statistical accuracy. Hence less concentrated systems, such as LHCEs for example, require much larger simulations to enable the same accuracy level as the analysis results of a HCE which more or less disqualify AIMD for such systems.

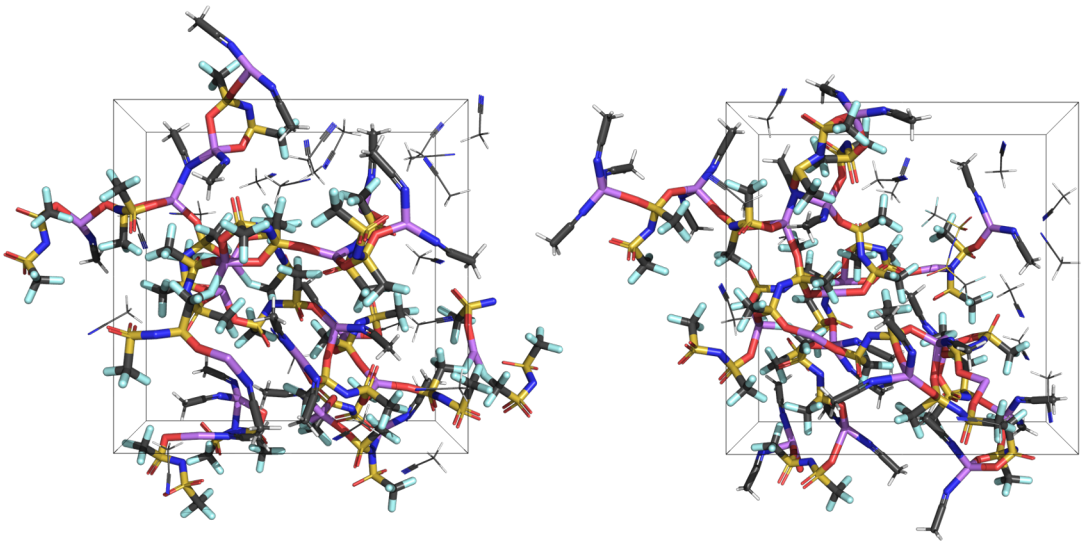

Figure 5.3: Snapshots of the periodic simulation cell, highlighting the percolating network in a sea of solvent.

5.3 Generated Force Fields

To use the CHAMPION method to the full extent large simulations must be utilised. For systems that would benefit the most from being studied by the CHAMPION method (HCE, LHCE, *etc.*) FFs usually do not capture the correct dynamics, hence not allowing for these systems to be studied through MD simulations [13]. Paper **III** focuses on extending the functionality of the CHAMPION method by combining it with the insights gained in Åvall & Johansson 2020 [19]. The quality of the FF generated depends heavily on the number of bins n (Fig. 5.4). To overcome this hurdle a large enough number of bins was chosen after converging such that it was unlikely that the bin size would affect the mean force values to a larger extent. Then the data was used to generate a GP regression model. To ensure that the correct interactions were captured the data was divided in two halves, where the first half start from an unequilibrated state, and the second half starts where the first ends (Fig. 5.5). As seen the method capture the same physics at both long and short range, indicating that correct electrostatics as well as dispersion is found.
However even though we see that the GP regression take the same form for both the equilibrated and unequilibrated data (Fig. 5.5) using these FFs deteriorate a simulation after only a few time steps. These FF curves were generated by sampling the data every 10 fs. This yields an incredibly low statistical inefficiency s (table 5.6), hence the number of time steps for which a force correlations effectively persist is on the scale of ~ 1. Sampling the data every 0.1 fs yields a higher correlation of the forces, hence, when calculating forces using finite difference, the forces should be more accurate when compared to ones yielded using a longer time step, and in turn indicate that the simulation will not melt or explode for a larger number of time steps.
No parameter besides Δt should affect s, however since this quality is measured through a curve fit there is not an exact measurement, hence the order of magnitude

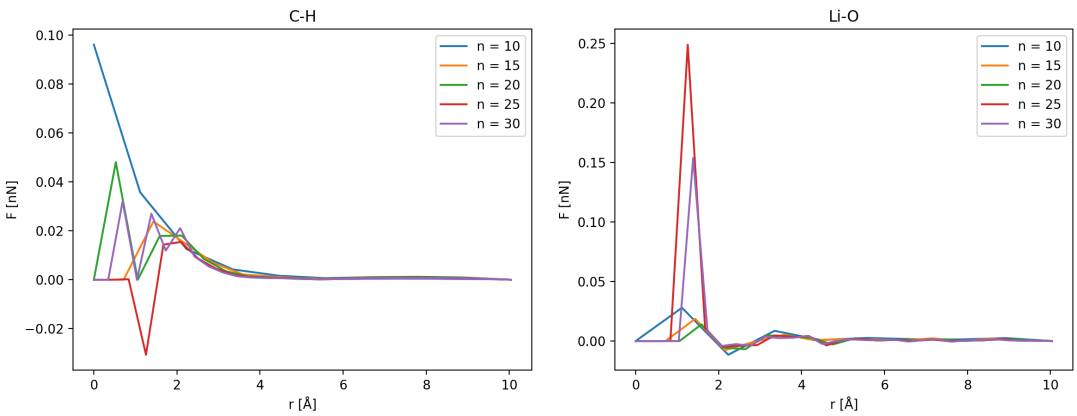

(a) How the C-H force field depends on the number of bins n.

(b) How the Li-O force field depends on the number of bins n.

Figure 5.4: Comparing the quality of the generalised Åvall FF depend on number of bins.

is more important than the specific number and the measured values in table 5.6 should be seen as a rough estimate.
When sampling every 0.1 fs for finite difference calculations of forces (Fig. 5.7) the magnitude of forces are more similar to literature [19] than when sampling every 10.0 fs. However there is a large discrepancy of one to two orders of magnitude. This discrepancy makes it apparent that finite difference used still does not capture the true dynamics, which is also apparent since MD simulations using these FFs melt. Note though that at present these results are under development, which underpins the discussion here.

Moving forward the data collection has to be changed to solve the issue caused by using a finite difference method to obtain forces. Worth noting is that the error bars (Fig 5.7) are small, indicating that the data could be separated in such a manner that *e.g.* linearly bonded C-C and cyclically bonded C-C can obtain their own FF term. The fact that different geometries does not at the moment obtain their own term can of course also contribute to the erroneous results, especially since this could explain the multi-peak nature of the FFs. Nonetheless more work is needed to tune this method.

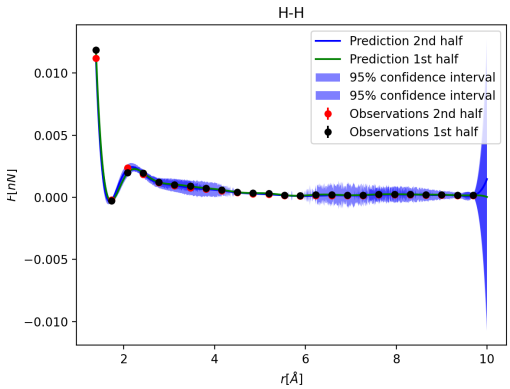

(a) A force field generated for H-H interaction using Gaussian Process regression for the 1st and 2nd half of a simulation trajectory.

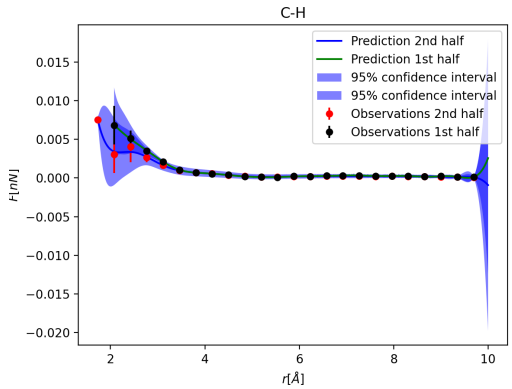

(b) A force field generated for C-H interaction using Gaussian Process regression for the 1st and 2nd half of a simulation trajectory.

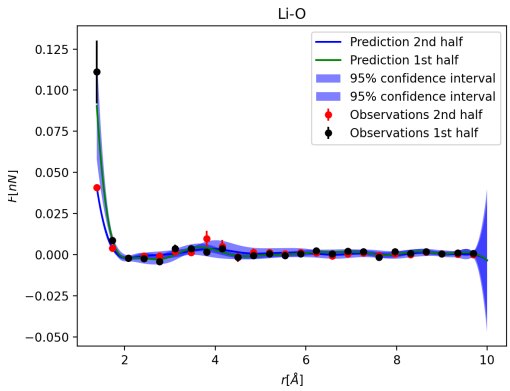

(c) A force field generated for Li-O interaction using Gaussian Process regression for the 1st and 2nd half of a simulation trajectory.

Figure 5.5: The form of the Åvall FF after using the raw data as input to a Gaussian Process regression. The same physics is captured when studying the 1st half of a simulation as when studying the 2nd half.

Table 5.6: The *statistical inefficiency* s dependence on Δt, the number of time steps $N_{timesteps}$, and the graph radius d.

Δt[fs]	$N_{\text{time step}}$	d	s
10.0	60218	3	1.869
0.1	1000	3	22.7221
0.1	10000	3	72.0633
0.1	10000	1	35.3487
0.1	5000	1	21.1608

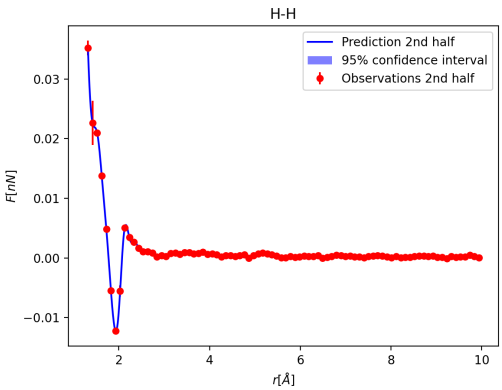

(a) A force field generated for H-H interaction using Gaussian Process regression based on data with a statistical inefficiency $s = 21.1608$.

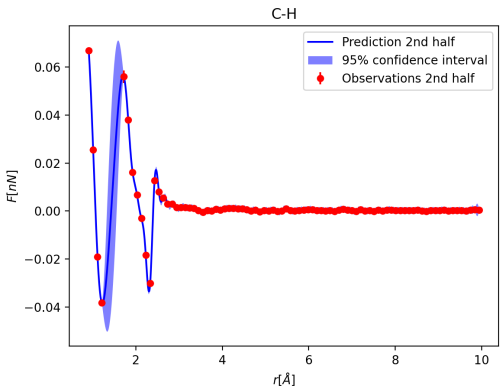

(b) A force field generated for C-H interaction using Gaussian Process regression based on data with a statistical inefficiency $s = 21.1608$.

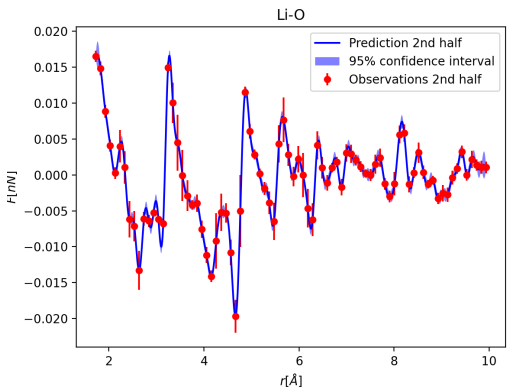

(c) A force field generated for Li-O interaction using Gaussian Process regression based on data with a statistical inefficiency $s = 21.1608$.

Figure 5.7: The form of the Åvall FF after using the raw data as input to a Gaussian Process regression. Data with a statistical inefficiency $s = 21.1608$.

6
Conclusion & Outlook

This thesis has studied battery electrolytes using computational means at different scales, and tied together these scales through the development of a new method. In paper **I** and **II** the importance of studying one scale to understand another is showcased. In paper **I** through seeing that the local structure of HCEs are retained in LHCEs, and from this being able to create hypotheses regarding macroscopic properties. Similarly in paper **II** through understanding how the local structure gives rise to the global structure, and how the global structure can be used to explain transport properties. These two papers exemplify how computational methods open up a future where materials science can be made more effective and predictive.

In order to enable such predictions using the CHAMPION [46] framework large scale MD simulations have to be easily available. In paper **III** the development of a method trying to tackle this problem was initiated, however much work is still needed on this method. Moving forward it would be interesting to fine tune the FF by adding on bonded terms, ensuring that molecular shape is retained more accurately. Besides adding bonded terms the immediate calls to action to improve the method presented in this thesis are:

- Use AIMD forces instead of finite difference generated forces.
- Separate interactions based on local structure rather than solely on participating elements.
- Enable a reactive FF for bonded terms.

Given all these pieces it would be interesting to study large scale simulations of LHCEs and studying how these systems behave and what structures form on a global scale. Especially the cumulative effects when large scale MD simulations for any material quickly and cost effectively is combined with the CHAMPION analysis. Through such endeavours it will be most interesting, seeing what physical properties can be explained this way. These types of studies should enable probing the phase separation between the diluent and the HCE structures, making it possible to study cluster formation, and cluster size, transport phenomena *etc.* Similarly the combination of the methods presented in this thesis could provide an avenue to study electrolyte-electrode interface and interphase interactions. From there on it is up to the imagination of the reader to find interesting problems where these methods can be applied.

Acknowledgements

I would like to start by thanking my supervisor Professor Patrik Johansson for giving me the freedom to pursue research freely, and for all the support in writing this thesis. Secondly Professor Aleksandar Matic, my examiner and closest boss, thank you for keeping spirits up around MF both online and offline during these trying times. Thank you Dr. Rasmus Andersson for your continuous support, friendship, and rubber ducking. Without the discussions you and I have had throughout the years we would not be where we are now. I would also like to thank all the colleagues at MF that have come and gone throughout the years, you make the PhD candidate life easier and I hope we can start hanging out face to face again soon. In addition I would like to send a big thank you to Victor Westergård and Peter Deaking at Chalmers Innovation office for all help with patenting our insights. Lastly I would like to thank Emil Krutmeijer, Johannes Henriksson, and Rasmus yet again, my teammates at Compular, the ball is rolling let's keep it up! Also thank you Bo, hopefully you'll be back soon! I would also like to show my appreciation to my funders, Energimyndigheten and the CARBAT project for enabling it all as well as the Swedish National Infrastructure for Computing (SNIC) for providing my work with computational resources.

Fabian Årén, Gothenburg, August 2021

Bibliography

[1] P.-A. Martin, F. Årén, and P. Johansson. Localized Highly Concentrated Electrolytes for Calcium Batteries. In manuscript.

[2] R Andersson, F Årén, A Franco, and P Johansson. Ion transport mechanisms via time-dependent local structure and dynamics in highly concentrated electrolytes. *Journal of the Electrochemical Society*, 167(14):140537, 2020.

[3] F. Årén, R. Andersson, and P. Johansson. Learning Force Fields from *Ab initio* Data. In manuscript.

[4] Jeff McMahon. Why Energy Storage Is Proving Even More Disruptive Than Cheap Renewables. Section: Sustainability.

[5] George E. Blomgren. The Development and Future of Lithium Ion Batteries. *J. Electrochem. Soc.*, 164(1):A5019–A5025, January 2017. Number: 1 Reporter: J. Electrochem. Soc.

[6] Noorullah Kuchai, Paul Shepherd, Juliana Calabria-Holley, Alexander Copping, Aude Matard, and David Coley. The potential for computational IT tools in disaster relief and shelter design. *Journal of International Humanitarian Action*, 5(1):1, April 2020.

[7] Aanchal Mongia, Sanjay Kr Saha, Emilie Chouzenoux, and Angshul Majumdar. A computational approach to aid clinicians in selecting anti-viral drugs for COVID-19 trials. *Scientific Reports*, 11(1):9047, April 2021. Number: 1 Publisher: Nature Publishing Group.

[8] The Nobel Prize in Chemistry 1998.

[9] B. J. Alder and T. E. Wainwright. Studies in molecular dynamics. i. general method. *The Journal of Chemical Physics*, 31(2):459–466, 1959.

[10] J. B. Gibson, A. N. Goland, M. Milgram, and G. H. Vineyard. Dynamics of radiation damage. *Phys. Rev.*, 120:1229–1253, Nov 1960.

[11] The Nobel Prize in Chemistry 2013.

[12] Sang-Pil Kim, Adri C. T. van Duin, and Vivek B. Shenoy. Effect of electrolytes on the structure and evolution of the solid electrolyte interphase (SEI) in Li-ion batteries: A molecular dynamics study. *Journal of Power Sources*, 196(20):8590–8597, 2011.

[13] Dmitry Bedrov, Jean-Philip Piquemal, Oleg Borodin, Alexander D MacKerell Jr, Benoît Roux, and Christian Schröer. Molecular dynamics simulations of ionic liquids and electrolytes using polarizable force fields. *Chemical reviews*, 119(13):7940–7995, 2019.

[14] Bharath Ravikumar, Mahesh Mynam, and Beena Rai. Effect of salt concentration on properties of lithium ion battery electrolytes: a molecular

dynamics study. *The Journal of Physical Chemistry C*, 122(15):8173–8181, 2018.

[15] Pilsun Yoo, Michael Sakano, Saaketh Desai, Md Mahbubul Islam, Peilin Liao, and Alejandro Strachan. Neural network reactive force field for c, h, n, and o systems. *npj Computational Materials*, 7(1):1–10, 2021.

[16] Justin S Smith, Olexandr Isayev, and Adrian E Roitberg. Ani-1: an extensible neural network potential with dft accuracy at force field computational cost. *Chemical science*, 8(4):3192–3203, 2017.

[17] Han-Xiao Li, Xu-Yuan Zhou, Yue-Chao Wang, and Hong Jiang. Theoretical study of na+ transport in the solid-state electrolyte na 3 obr based on deep potential molecular dynamics. *Inorganic Chemistry Frontiers*, 8(2):425–432, 2021.

[18] Davide Castelvecchi. Can we open the black box of ai? *Nature News*, 538(7623):20, 2016.

[19] Gustav Åvall and Patrik Johansson. A novel approach to ligand-exchange rates applied to lithium-ion battery and sodium-ion battery electrolytes. *The Journal of chemical physics*, 152(23):234104, 2020.

[20] Amin Mahmoudzadeh Andwari, Apostolos Pesiridis, Srithar Rajoo, Ricardo Martinez-Botas, and Vahid Esfahanian. A review of battery electric vehicle technology and readiness levels. *Renewable and Sustainable Energy Reviews*, 78:414–430, 2017.

[21] Yeru Liang, Chen-Zi Zhao, Hong Yuan, Yuan Chen, Weicai Zhang, Jia-Qi Huang, Dingshan Yu, Yingliang Liu, Maria-Magdalena Titirici, Yu-Lun Chueh, et al. A review of rechargeable batteries for portable electronic devices. *InfoMat*, 1(1):6–32, 2019.

[22] Helena Berg. *Batteries for electric vehicles: materials and electrochemistry*. Cambridge university press, 2015.

[23] John B Goodenough and Youngsik Kim. Challenges for rechargeable li batteries. *Chemistry of materials*, 22(3):587–603, 2010.

[24] M. Elena Arroyo-de Dompablo, Alexandre Ponrouch, Patrik Johansson, and M. Rosa Palacín. Achievements, challenges, and prospects of calcium batteries. *Chemical Reviews*, 120(14):6331–6357, 2020. PMID: 31661250.

[25] Alexandre Ponrouch, Jan Bitenc, Robert Dominko, Niklas Lindahl, Patrik Johansson, and M Rosa Palacín. Multivalent rechargeable batteries. *Energy Storage Materials*, 20:253–262, 2019.

[26] Lorenzo Stievano, Iratxe de Meatza, Jan Bitenc, Carmen Cavallo, Sergio Brutti, and Maria Assunta Navarra. Emerging calcium batteries. *Journal of Power Sources*, 482:228875, 2021.

[27] Alexandre Ponrouch, C Frontera, Fanny Bardé, and M Rosa Palacín. Towards a calcium-based rechargeable battery. *Nature materials*, 15(2):169–172, 2016.

[28] Akiko Tsurumaki, Marco Agostini, Ruggero Poiana, Lucia Lombardo, Ernestino Lufrano, Cataldo Simari, Aleksandar Matic, Isabella Nicotera, Stefania Panero, and Maria Assunta Navarra. Enhanced safety and galvanostatic performance of high voltage lithium batteries by using ionic liquids. *Electrochimica Acta*, 316:1–7, 2019.

[29] MM Kabir and Dervis Emre Demirocak. Degradation mechanisms in li-ion batteries: a state-of-the-art review. *International Journal of Energy Research*, 41(14):1963–1986, 2017.

[30] Gaoxue Jiang, Fang Li, Huaping Wang, Mingguang Wu, Shihan Qi, Xinhua Liu, Shichun Yang, and Jianmin Ma. Perspective on high-concentration electrolytes for lithium metal batteries. *Small Structures*, page 2000122.

[31] Yuki Yamada, Keizo Furukawa, Keitaro Sodeyama, Keisuke Kikuchi, Makoto Yaegashi, Yoshitaka Tateyama, and Atsuo Yamada. Unusual stability of acetonitrile-based superconcentrated electrolytes for fast-charging lithium-ion batteries. *Journal of the American Chemical Society*, 136(13):5039–5046, 2014.

[32] R Petibon, CP Aiken, L Ma, D Xiong, and JR Dahn. The use of ethyl acetate as a sole solvent in highly concentrated electrolyte for li-ion batteries. *Electrochimica Acta*, 154:287–293, 2015.

[33] Dennis W McOwen, Daniel M Seo, Oleg Borodin, Jenel Vatamanu, Paul D Boyle, and Wesley A Henderson. Concentrated electrolytes: decrypting electrolyte properties and reassessing al corrosion mechanisms. *Energy & Environmental Science*, 7(1):416–426, 2014.

[34] Viktor Nilsson, Diana Bernin, Daniel Brandell, Kristina Edström, and Patrik Johansson. Interactions and transport in highly concentrated litfsi-based electrolytes. *ChemPhysChem*, 21(11):1166–1176, 2020.

[35] Daniel M Seo, Oleg Borodin, Daniel Balogh, Michael O'Connell, Quang Ly, Sang-Don Han, Stefano Passerini, and Wesley A Henderson. Electrolyte solvation and ionic association iii. acetonitrile-lithium salt mixtures–transport properties. *Journal of The Electrochemical Society*, 160(8):A1061, 2013.

[36] Jiangfeng Qian, Wesley A Henderson, Wu Xu, Priyanka Bhattacharya, Mark Engelhard, Oleg Borodin, and Ji-Guang Zhang. High rate and stable cycling of lithium metal anode. *Nature communications*, 6(1):1–9, 2015.

[37] Xiulin Fan, Xiao Ji, Fudong Han, Jie Yue, Ji Chen, Long Chen, Tao Deng, Jianjun Jiang, and Chunsheng Wang. Fluorinated solid electrolyte interphase enables highly reversible solid-state li metal battery. *Science advances*, 4(12):eaau9245, 2018.

[38] Ji Chen, Qin Li, Travis P Pollard, Xiulin Fan, Oleg Borodin, and Chunsheng Wang. Electrolyte design for li metal-free li batteries. *Materials Today*, 39:118–126, 2020.

[39] Yu Zheng, Fernando A Soto, Victor Ponce, Jorge M Seminario, Xia Cao, Ji-Guang Zhang, and Perla B Balbuena. Localized high concentration electrolyte behavior near a lithium–metal anode surface. *Journal of Materials Chemistry A*, 7(43):25047–25055, 2019.

[40] Yu Zheng, Fernando A. Soto, Victor Ponce, Jorge M. Seminario, Xia Cao, Ji-Guang Zhang, and Perla B. Balbuena. Localized high concentration electrolyte behavior near a lithium–metal anode surface. *J. Mater. Chem. A*, 7:25047–25055, 2019.

[41] Xia Cao, Xiaodi Ren, Lianfeng Zou, Mark H Engelhard, William Huang, Hansen Wang, Bethany E Matthews, Hongkyung Lee, Chaojiang Niu, Bruce W Arey, et al. Monolithic solid–electrolyte interphases formed in fluorinated

orthoformate-based electrolytes minimize li depletion and pulverization. *Nature Energy*, 4(9):796–805, 2019.

[42] Amine Bouibes, Soumen Saha, and Masataka Nagaoka. Theoretically predicting the feasibility of highly-fluorinated ethers as promising diluents for non-flammable concentrated electrolytes. *Scientific reports*, 10(1):1–10, 2020.

[43] Da Wang, Xiangwen Gao, Yuhui Chen, Liyu Jin, Christian Kuss, and Peter G Bruce. Plating and stripping calcium in an organic electrolyte. *Nature materials*, 17(1):16–20, 2018.

[44] D Aurbach, R Skaletsky, and Y Gofer. The electrochemical behavior of calcium electrodes in a few organic electrolytes. *Journal of the Electrochemical Society*, 138(12):3536, 1991.

[45] Satoshi Uchida and Tetsu Kiyobayashi. How does the solvent composition influence the transport properties of electrolyte solutions? lipf 6 and lifsa in ec and dmc binary solvent. *Physical Chemistry Chemical Physics*, 23(18):10875–10887, 2021.

[46] Rasmus Andersson, Fabian Årén, Alejandro A. Franco, and Patrik Johansson. Champion: Chalmers hierarchical atomic, molecular, polymeric and ionic analysis toolkit. *Journal of Computational Chemistry*, n/a(n/a).

[47] E Weinan. *Principles of multiscale modeling*. Cambridge University Press, 2011.

[48] Paul Adrien Maurice Dirac. Quantum mechanics of many-electron systems. *Proceedings of the Royal Society of London. Series A, Containing Papers of a Mathematical and Physical Character*, 123(792):714–733, 1929.

[49] Michael A Nielsen and Isaac Chuang. Quantum computation and quantum information, 2002.

[50] Jos Thijssen. *Computational physics*. Cambridge university press, second edition, 2007.

[51] Yan Zhao and Donald G. Truhlar. The M06 suite of density functionals for main group thermochemistry, thermochemical kinetics, noncovalent interactions, excited states, and transition elements: two new functionals and systematic testing of four M06-class functionals and 12 other functionals. *Theoretical Chemistry Accounts*, 120(1):215–241, May 2008.

[52] K. Kim and K. D. Jordan. Comparison of Density Functional and MP2 Calculations on the Water Monomer and Dimer. *The Journal of Physical Chemistry*, 98(40):10089–10094, October 1994. Publisher: American Chemical Society.

[53] Richard Car and Mark Parrinello. Unified approach for molecular dynamics and density-functional theory. *Physical review letters*, 55(22):2471, 1985.

[54] Jürg Hutter and Marcella Iannuzzi. Cpmd: Car-parrinello molecular dynamics. *Zeitschrift für Kristallographie-Crystalline Materials*, 220(5-6):549–551, 2005.

[55] David A Case, Thomas E Cheatham III, Tom Darden, Holger Gohlke, Ray Luo, Kenneth M Merz Jr, Alexey Onufriev, Carlos Simmerling, Bing Wang, and Robert J Woods. The amber biomolecular simulation programs. *Journal of computational chemistry*, 26(16):1668–1688, 2005.

[56] Bernard R Brooks, Charles L Brooks III, Alexander D Mackerell Jr, Lennart Nilsson, Robert J Petrella, Benoît Roux, Youngdo Won, Georgios Archontis,

Christian Bartels, Stefan Boresch, et al. Charmm: the biomolecular simulation program. *Journal of computational chemistry*, 30(10):1545–1614, 2009.

[57] Mark James Abraham, Teemu Murtola, Roland Schulz, Szilárd Páll, Jeremy C Smith, Berk Hess, and Erik Lindahl. Gromacs: High performance molecular simulations through multi-level parallelism from laptops to supercomputers. *SoftwareX*, 1:19–25, 2015.

[58] Jörg Behler and Michele Parrinello. Generalized neural-network representation of high-dimensional potential-energy surfaces. *Physical review letters*, 98(14):146401, 2007.

[59] Albert P Bartók, Mike C Payne, Risi Kondor, and Gábor Csányi. Gaussian approximation potentials: The accuracy of quantum mechanics, without the electrons. *Physical review letters*, 104(13):136403, 2010.

[60] Albert P Bartók, Risi Kondor, and Gábor Csányi. On representing chemical environments. *Physical Review B*, 87(18):184115, 2013.

[61] Kristof T Schütt, Huziel E Sauceda, P-J Kindermans, Alexandre Tkatchenko, and K-R Müller. Schnet–a deep learning architecture for molecules and materials. *The Journal of Chemical Physics*, 148(24):241722, 2018.

[62] Wujie Wang, Tzuhsiung Yang, William H Harris, and Rafael Gómez-Bombarelli. Active learning and neural network potentials accelerate molecular screening of ether-based solvate ionic liquids. *Chemical Communications*, 56(63):8920–8923, 2020.

[63] Peter Meltzer, Marcelo Daniel Gutierrez Mallea, and Peter J Bentley. Pinet: A permutation invariant graph neural network for graph classification. *arXiv preprint arXiv:1905.03046*, 2019.

[64] Lisanne Knijff and Chao Zhang. Machine learning inference of molecular dipole moment in liquid water. *arXiv preprint arXiv:2103.08274*, 2021.

[65] BIG-MAP.

[66] Materials Genome Initiative | WWW.MGI.GOV.

[67] Kang Xu. Nonaqueous liquid electrolytes for lithium-based rechargeable batteries. *Chemical reviews*, 104(10):4303–4418, 2004.

[68] Kang Xu. Electrolytes and interphases in li-ion batteries and beyond. *Chemical reviews*, 114(23):11503–11618, 2014.

[69] Daniel M Seo, Oleg Borodin, Sang-Don Han, Paul D Boyle, and Wesley A Henderson. Electrolyte solvation and ionic association ii. acetonitrile-lithium salt mixtures: highly dissociated salts. *Journal of The Electrochemical Society*, 159(9):A1489, 2012.

[70] Yuki Yamada and Atsuo Yamada. Superconcentrated electrolytes for lithium batteries. *Journal of The Electrochemical Society*, 162(14):A2406, 2015.